Initial Cone-in-Shell, Fast-Ignition Experiments on OMEGA

Introduction

Fast ignition[1,2] is an attractive option for inertial confinement fusion because the target compression and ignition stages are separated, relaxing the requirements on the symmetry of the implosion and the compression energy. Massive fuel shells can be imploded with low velocity, providing the potential of higher gains at lower total driver energy than in conventional central hot-spot ignition schemes.[3] In fast ignition, the dense core is ignited by particles (electrons, protons, or ions) generated by a short, ultra-intense, high-energy laser pulse. Fast ignition relies on the localized deposition of the particle energy in the core. Design studies have been performed for electrons with integrated simulations coupling a hydrodynamic code with a hybrid particle-in-cell (PIC) code.[4] The simulations estimate that electron-beam energies ranging from ~40 to 100 kJ are required for ignition, assuming a Gaussian-shaped fast-electron beam with an ~30-μm spot size, a 10-ps duration, and a relativistic Maxwellian distribution with ~2-MeV mean energy. The beam is injected 125 μm from the target center into a compressed DT core with $\rho \sim 500$-g/cm^3 peak density and $\rho R \sim 1$-g/cm^2 areal density.[4] The ignition threshold depends on the initial beam's full-divergence angle, which was varied from 40° to 80° in the simulation. Similar ignition electron-beam energies have been obtained in other design studies.[5,6] These design studies are still lacking a detailed description of the laser–plasma interaction, which is complex and will require massive, large-scale, three-dimensional (3-D) PIC simulations.[7]

Maximizing the coupling efficiency of the short-pulse energy into core heating remains a challenge for full-scale fast ignition. The conversion efficiency of fast electrons with the appropriate energy (1 to 2 MeV) needs to be maximized, and the particles must be transported efficiently from their source location to the compressed fuel, where they must be stopped in a sufficiently small volume that matches the optimal size of the ignition spark. Self-generated resistive magnetic fields are predicted to significantly affect the transport of hot electrons.[8,9] A self-generated magnetic field may collimate the beam as a whole while it propagates into the dense core and, therefore, may increase the coupling efficiency.[10]

It is important to bring the fast-electron source as close as possible to the fuel assembly. A very promising approach is the cone-in-shell concept[11] with encouraging initial integrated experiments at the GEKKO Laser Facility, which reported significant heating by a 0.6-ps, 300-J short-pulse laser.[12] The re-entrant cone makes it possible for a high-energy petawatt laser pulse to propagate as close as possible to the dense core, avoiding the need to channel the laser beam through a large region of plasma material.

Figure 125.12 shows a schematic of the integrated cone-in-shell, fast-ignitor experiments reported here, which were conducted at the Omega Laser Facility,[13] including the short-pulse OMEGA EP laser.[14] The coupling efficiency will depend on the separation of the cone tip from the dense plasma. A shorter distance will increase the hydrodynamic forces on the cone tip, which result from a jet formed by imploded plasma impacting the cone tip and launching a shock wave through the tip. This shock wave must not break out from the inner cone surface before the short pulse is fired; otherwise, plasma will quickly fill the cone, significantly increasing the electron-propagation distance and lowering the transport efficiency.
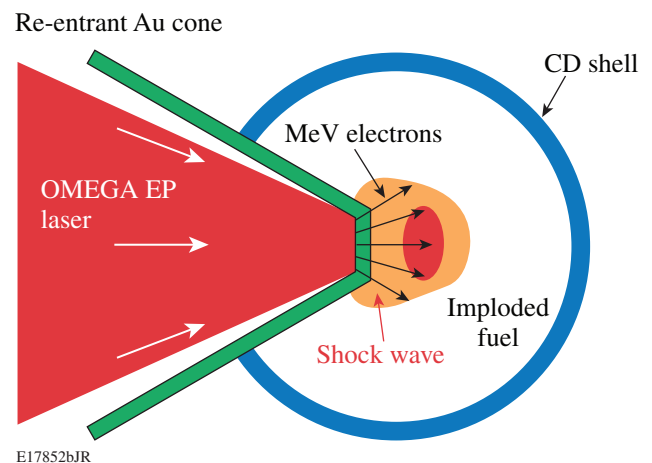

E17852bJR

Figure 125.12
Schematic of the integrated cone-in-shell, fast-ignition experiment.

Design studies and experiments are needed to determine the optimum separation distance, tip thickness, and cone wall material. The shell mass and implosion velocity will have a significant effect on the force that the plasma jet exerts on the cone tip. It has been shown that low-velocity implosions of massive shells on a low adiabat lead to a cold and dense fuel assembly that is ideal for fast ignition.[3] The resulting dense core has a relatively low pressure and large size, reducing the hydrodynamic forces and creating a smaller distance between the tip and the dense core edge. Spherical symmetric low-adiabat implosions of cryogenic targets in direct-drive geometry have been demonstrated on OMEGA with triple-picket laser pulses, achieving a neutron-rate–averaged areal density (ρR) of up to 300 mg/cm^2 (Ref. 15).

This article describes initial integrated fast-ignition experiments at the Omega Laser Facility, which uses low-adiabat implosions and demonstrates core heating with a 1-kJ, 10-ps, short-pulse laser. Companion experiments demonstrate that the cone tip is intact at the time when the short-pulse laser is fired into the cone. The integrated experiments produced up to ~1.4×10^7 additional neutrons.

The following sections describe the targets and the laser setup; discuss shock-breakout measurements, the integrated fast-electron heating experiment, and the integrated simulations; and conclude with a summary.

Targets and Laser Setup

The targets were relatively thick walled (40-μm), ~870-μm-outer-diam deuterated-plastic (CD) shells with an inserted hollow gold cone; they were fabricated and characterized by General Atomics.[16] Figure 125.13(a) is a photograph of a target mounted on a support stalk; Fig. 125.13(b) shows a target cross section with target dimensions. A shelf is machined into the gold cone to attach the shell. This serves as a reference for placing the tip precisely in the desired location, 40±10 μm away from the center of the shell along the cone axis. The shell was not filled with gas for these experiments. An x-ray radiograph of such a target can be found in Ref. 17. The cone has an inner full opening angle of 34±1°, a side-wall thickness of 10 μm, and a small circular flat tip. The cone wall is 50 μm thick outside the shell. The tip diameter was either 10 or 40 μm. The tip thickness was 5, 10, or 15 μm in the shock-breakout experiment described in **Shock-Breakout Measurements**, p. 15 and 10 or 15 μm in the integrated shots discussed in **Integrated Fast-Electron–Heating Experiments**, p. 17.

The shells were imploded on an adiabat of $\alpha_{in} \approx 1.5$ (Ref. 18), where α_{in} is defined as the ratio of plasma pressure in the inner portion of the shell to the Fermi pressure of a fully degenerate electron gas. Figure 125.14 shows the ~2.7-ns drive pulse, consisting of a 90-ps full-width-at-half-maximum (FWHM) Gaussian prepulse with ~6.5 TW of peak power attached to a shaped main pulse with a foot power of ~0.8 TW and a peak power of ~12 TW. The shell was imploded using 54 out of the 60 UV OMEGA beams with a total energy of ~20 kJ. The laser light was smoothed with polarization rotators and distributed phase plates.[19,20]

The fuel assembly was optimized in previous work,[18,21] with a predicted peak ρR of ~0.4 g/cm^2 and ρ_{max} of ~150 g/cm^3 for an empty-shell target. Secondary proton measurements with symmetrically irradiated 40-μm spherical plastic shells filled
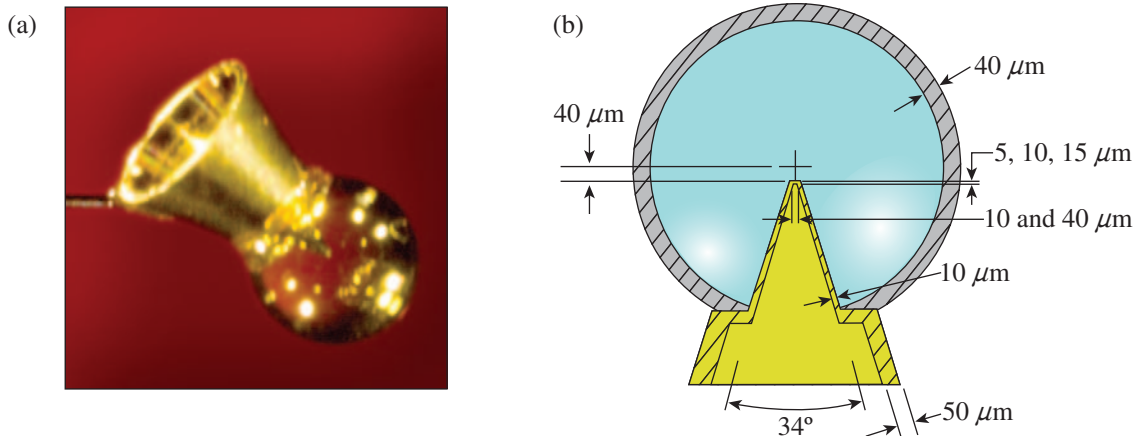
E19548JR

Figure 125.13
(a) Photograph of a gold re-entrant cone target; (b) cross-sectional drawing through the shell and cone tip with target dimensions.
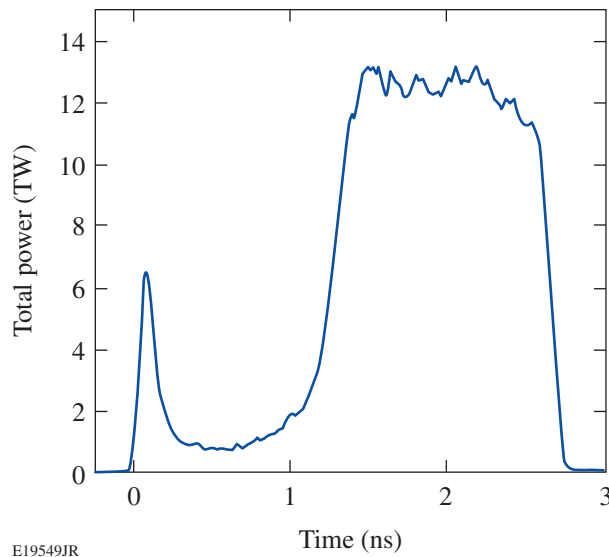
Figure 125.14
Drive-laser pulse shape (shot 55154).

with 25 atm of D_2 gas demonstrated a fuel assembly close to the 1-D prediction, a measured neutron-averaged ρR of 0.15 g/cm^2, and a peak ρR of 0.26 g/cm^2 (Ref. 18).

The 1053-nm–wavelength short pulse from the OMEGA EP laser had an energy of ~1 kJ and a 10-ps duration and was focused to a spot with a radius of R_{80} = (26±2) μm and containing 80% of the laser energy. A high-resolution wavefront sensor measured the on-shot fluence distribution in the focal plane of the OMEGA EP pulse at full energy.[22] More than 30% of the laser energy had an intensity $>1 \times 10^{19}$ W/cm^2, while the average intensity within R_{80} was $(6\pm2) \times 10^{18}$ W/cm^2. The focal pattern and R_{80} varied slightly from shot to shot. A picture of the focal spot can be found in Ref. 23.

A high laser contrast, defined as the ratio of the peak power to the power of the pedestal before the main pulse, is critical for cone-in-shell fast ignition,[24] requiring careful characterization of the prepulse. A nanosecond prepulse caused by front-end parametric fluorescence preceded the OMEGA EP pulse, which was spatially and temporally resolved.[25] The on-shot temporal contrast was measured with a set of calibrated fast photodiodes. The measured power and energy contrast were $(3.1\pm0.5) \times 10^6$ and $(4.6\pm0.9) \times 10^4$, respectively, leading to a prepulse energy of ~22 mJ for a 1-kJ main-pulse energy. The prepulse is described by a Gaussian with FWHM of 0.9 ns and a peak 1 ns before the main pulse. [See Fig. 1(b) in Ref. 23.] The focal spot of the prepulse was measured to have a diameter of 39±3.5-μm FWHM, resulting in a prepulse intensity of $(1.7\pm0.4) \times 10^{12}$ W/cm^2.

Shock-Breakout Measurements

The compressing shell pushes a jet of plasma material toward the cone tip,[17] heating the plasma to a temperature >1 keV and creating a shock wave through the cone wall. Shock-breakout measurements[26] were performed by imploding the shell without a short-pulse beam, using targets with a 40-μm-diam flat tip and thicknesses between 5 and 15 μm (Fig. 125.15). When the shock wave reached the inner cone surface, it generated optical emission inside the hollow cone, which was measured and temporally resolved with a streaked optical pyrometer (SOP)[27] in the wavelength range ~600 to ~750 nm and a velocity interferometer system for any reflector (VISAR)[28] at a wavelength of 532 nm. Figure 125.15(b) shows the measured SOP signal as a function of time for a 14-μm-thick tip. The optical emission suddenly rises when the shock breaks out at 3.72 ns. SOP integrates over a time period of 150 ps, determined by the slit width and the sweep speed of the streak camera. The signal is differentiated with respect to time and the first peak determines shock breakout with an accuracy of ±30 ps.[27] VISAR achieves a higher precision of ±10 ps in measuring shock breakout because of a faster streak camera.[28] Figure 125.15(c) shows the time of shock breakout as a function of tip thickness. The red circles are the VISAR and the blue squares the SOP measurements. Except for one shot at 10 μm, there is good agreement between both diagnostics within their error bars. With increasing tip thickness, the breakout is delayed. For thicknesses of 10 and 15 μm, the shock-breakout time was 3.70±0.03 ns and 3.76±0.03 ns, respectively. The red line is a weighted fit through all the data points.

The implosion of the cone-in-shell target and the shock propagation through the cone wall were simulated with the 2-D hydrodynamics code *SAGE*[29] in cylindrical geometry. Figure 125.16 shows a sequence of frames with zoomed images of the cone tip at times around peak compression. The first frame at 3.46 ns shows an intact cone tip when the shock wave just starts to enter the cone wall. At 3.50 ns the shock has propagated about halfway through the cone wall, pushing the outside cone wall back by ~5 μm, but has not broken out at the inner wall. In the simulation, the shock breaks through at 3.54 ns, ~0.2 ns before the experimentally measured breakout time of 3.76 ns. After shock breakout, the cone is predicted to very rapidly fill up with plasma below solid density but above the critical density of the short-pulse laser. A run with a 10-μm flat tip shows very similar shock behavior and a slightly earlier (40 ps) breakout time. No breakout measurements are available for the 10-μm flat tip. Using the relative timing from the simulations and the absolute timing from the measurements, the breakout time for 10-μm flat and

(a) Schematic showing CD shell, Au cone, Shock wave, Optical emission, Streaked optical pyrometer, VISAR 1 and 2 streak cameras, 3ω drive beams, Imaging

(b) SOP signal plot with Shock labeled

(c) Shock breakout plot — SOP and VISAR, Time of peak neutron production
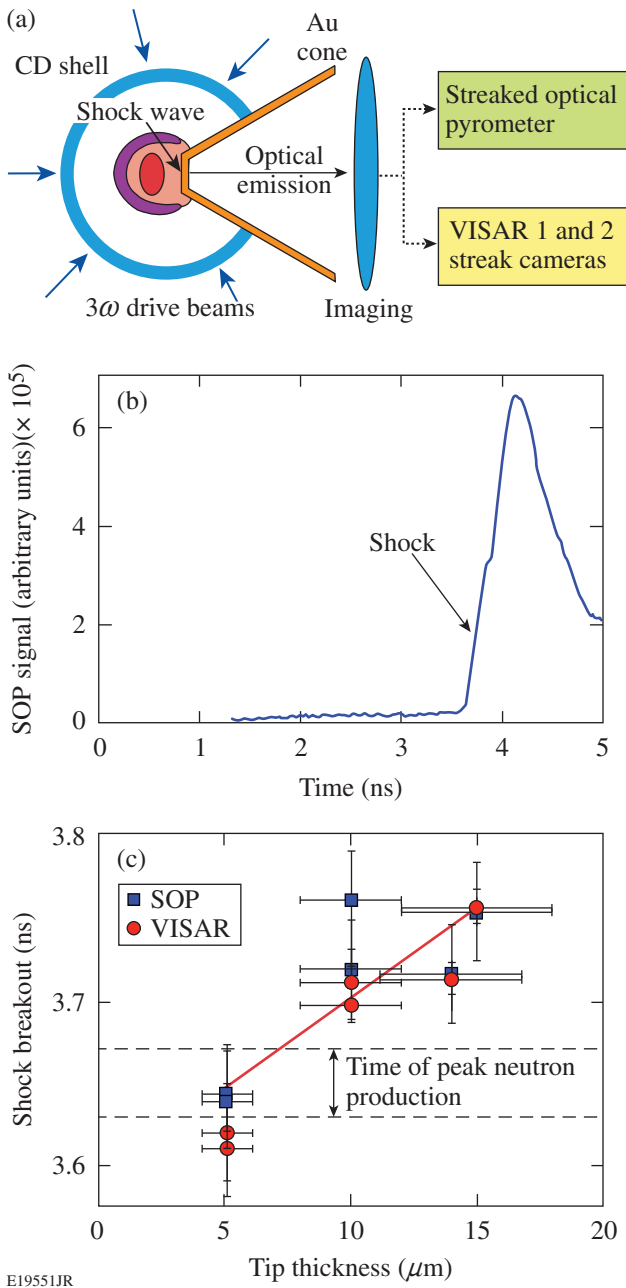
E19551JR

Figure 125.15

(a) Schematic of the shock-breakout experiment. The CD shell was imploded using just the long-pulse, 351-nm drive beams, resulting in shock propagation through the tip of the cone. Emergence of the shock at the inside of the tip was diagnosed using a streaked optical pyrometer (SOP) and VISAR. (b) SOP trace for a typical shot and (c) measured breakout time inside the cone for various tip thicknesses. The breakout is later for thicker cone tips.
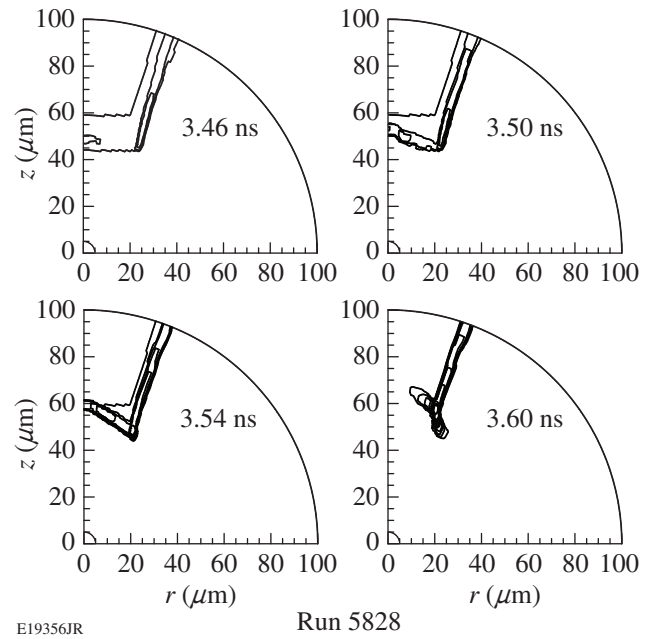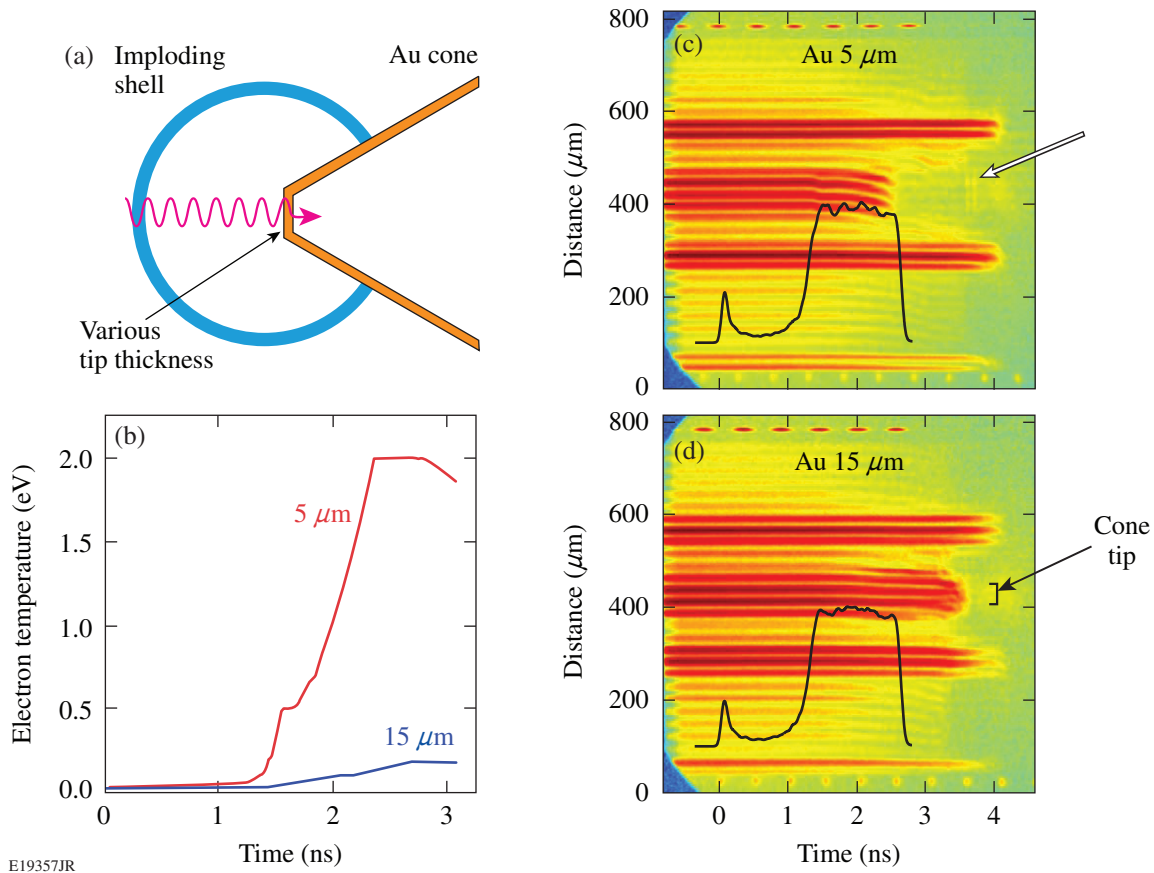

E19356JR   Run 5828

Figure 125.16

Sequence of density contours above 10 g/cm^3 in the tip of a Au cone from a 2-D *SAGE* simulation, showing the rapid propagation of a strong shock wave through a 15-μm cone tip. The fuel assembly from a cone-in-shell target (not shown) generates the shock. The shock propagates faster through the cone tip than through the wall.

Shock breakout appeared 70±36 ps after the peak of neutron production, confirming that the cone tip was intact at optimum OMEGA EP timing.

The VISAR measurements indicate that preheat can lead to a premature release of material inside the hollow cone if the cone wall is not thick enough. X-ray radiation in the ~5- to 10-keV photon range from the shell plasma can preheat the cone tip, as shown in Fig. 125.17(a). The temperature at the inside of the gold wall depends on the thickness of the tip. Figure 125.17(b) shows the electron temperature as a function of time for 5-μm and 15-μm thicknesses, calculated using the radiation hydrodynamic code *LILAC*.[30] *LILAC* modeled the x-ray production in the corona of the imploding shell during the drive pulse and its transport to the cone tip. At 1.5 ns, when the main-pulse intensity reaches its plateau, the temperature reaches ~0.5 eV or ~6000 K in the 5-μm case, while it is much lower for 15 μm. The temperature in the 5-μm tip is higher than the melting and boiling temperatures of gold, which are 1337 K and 3129 K (Ref. 31), respectively. Temperatures as high as ~2 eV or ~24,000 K are calculated at the end of the drive pulse are certainly sufficient to generate a gold plasma with a low degree of ionization. This effect is clearly observed in the VISAR measurement of Fig. 125.17(c).

15-μm-thick tip is extrapolated to 3.72±0.03 ns. This number is compared to the measured time of peak neutron production [see **Integrated Fast-Electron–Heating Experiments**, p. 17], which results in 3.65±0.02 ns for 10-μm flat, 15-μm-thick tips.

Figure 125.17
(a) Schematic for simulations of radiation preheat of the cone tip. Coronal x-ray radiation from the shell driven by the strong UV pulse can penetrate through the cone wall, preheating the gold material. (b) Calculated electron temperature at the inside of the cone tip for 5-μm and 15-μm thicknesses. (c) VISAR trace for a 5-μm thickness; the disappearance of the fringes at ~2.5 ns indicate preheat. The white arrow marks the optical emission at the shock-breakout time. (d) VISAR trace for a 15-μm thickness, showing no attenuation before shock breakout at 3.75 ns. The brace indicates the spatial range of the flat tip. In (c) and (d) the black curve indicates the laser's temporal shape.

The fringes are formed by a probe laser reflecting from the inside of the cone tip back into an interferometer. The VISAR diagnostic is a high-resolution optical imager that projects a magnified image (25.5×) of the inside of the cone onto the slits of a pair of streak camera detectors.[28] The system was aligned such that it imaged sharply the flat tip portion. The brace in Fig. 125.17(d) marks the spatial range, where fringes are formed through back reflection from that region. The two to three upper and lower fringes that remain up to 4 ns are due to reflection from the shelf in the cone. [See Fig. 125.13(b).] A fringe shift indicates a change in the optical path length with time, i.e., through a movement of the reflecting surface or through an increase in plasma density along the probe path. In Fig. 125.17(c) the fringes start to shift downward after the onset of the main pulse (black curve), indicating plasma formation within the cone. The velocity of the boundary of the gold plasma is predicted to steadily increase to ~5 × 10^5 cm/s at

3 ns, consistent with the observed fringe shift. With increasing ionization, a density gradient develops in front of the reflecting surface so that eventually the probe laser is completely absorbed, explaining the disappearance of the fringes at ~2.5 ns. For a 5-μm thickness, breakout is measured at 3.60 ns, based on two short vertical lines [marked by the white arrow in Fig. 125.17(c)] that are created by optical self-emission from the emerging shock wave at a wavelength of 532 nm. The two lines are exactly separated by the expected etalon delay[32] in the interferometer and provide a precise measurement of the breakout time. In contrast, the inner cone wall is well preserved for the 15-μm tip thickness, which is seen in Fig. 125.17(d), by the almost straight fringes up to the time of breakout.

Integrated Fast-Electron–Heating Experiments

In preparation for each integrated fast-ignition experiment, the short-pulse laser is precisely timed with respect to the drive

laser and pointed into the cone tip. The accuracy of pointing for the short-pulse laser is ~15 μm as measured by x-ray pinhole images.[21] The timing is measured *in situ* with ±30-ps precision at full energy by measuring the temporally resolved hard x-ray emission produced by the short-pulse laser interaction.[21] The main diagnostic for inferring the coupling efficiency of short-pulse laser energy into the compressed core is the yield of thermonuclear neutrons that are produced by d(d,n)^{3}He reactions. A new liquid-scintillator time-of-flight detector was developed to measure the neutron yield in the presence of a strong hard x-ray background from the short-pulse laser.[33] This was required because standard plastic scintillator detectors were overwhelmed by the hard x-ray radiation and did not provide a useful measurement in integrated shots.[33] The liquid scintillator detector completely suppresses the background at the time when the 2.45-MeV neutrons arrive and provides reliable neutron-yield data. The details of the new detector and background mitigation techniques in fast-ignition integrated experiments are discussed in Ref. 33. Examples of the measured neutron spectra are shown in Fig. 125.18 for different timings and two target types. The spectrum for an early arrival (3.52 ns) of the short-pulse laser is very similar to spectra obtained without the short-pulse laser. The spectrum at a later time (3.62 ns) for a 10-μm flat tip shows a significant enhanced neutron signal, while the increase is not as pronounced for the 40-μm flat tip (3.65 ns). No attempt was made to extract an ion temperature from the noisy and broadened spectra. This is because of (i) limited number of detected neutrons (~10 to 40 particles), (ii) neutron scattering by a 2.5-cm-thick lead plate that shielded x rays and was located in the line of sight and by other structures adjacent to the detector, and (iii) broadening effects from a relatively large (~3 liter) detector volume. The
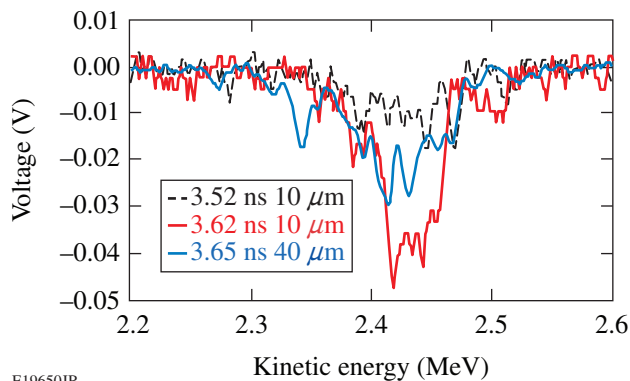
neutron time-of-flight spectra are integrated to provide a total yield. The neutron detector was cross calibrated against another absolutely calibrated neutron detector[34] using a series of shots without the short-pulse laser.

The implosion produces thermonuclear neutrons in the hot, dense core surrounded by the cold shell; but neutrons are also generated in the corona of the plasma. The whole shell was deuterated and the drive laser heated the region between the critical and the ablation surface to temperatures >1 keV, which generated a significant amount of neutrons outside the dense shell. The corona yield (0.73±0.08 × 10^7) was measured in a series of shots with cone-in-shell targets without the short-pulse laser, where the inside of the shell was coated with a CH plastic layer (1 to 5 μm) to quench the yield from the target center. The neutron yield was ~35% lower compared to pure CD shells and did not depend on the thickness of the CH layer. Previous experiments[35] showed that an inner 1-μm CH layer is sufficient to quench the fusion yield from the central region. Simulations show that fast-electron heating is insignificant in the region of the corona neutrons. The amount of fast-electron energy deposited in this region is negligible compared to the fast-electron energy coupled in the central plasma region. This justifies that the corona yield is treated as an offset and is subtracted from the measured yield.

Figure 125.19 shows the measured neutron yield as a function of the arrival time of the OMEGA EP pulse in the cone. Two types of targets were used. The red circles show the results for a 10-μm tip diameter and the blue triangles for a

Figure 125.18
Time-of-flight spectra of 2.45-MeV neutrons from thermonuclear d(d,n)^{3}He reactions in integrated fast-ignition experiments. Spectra with various timings of the OMEGA EP beam are shown for two target types.
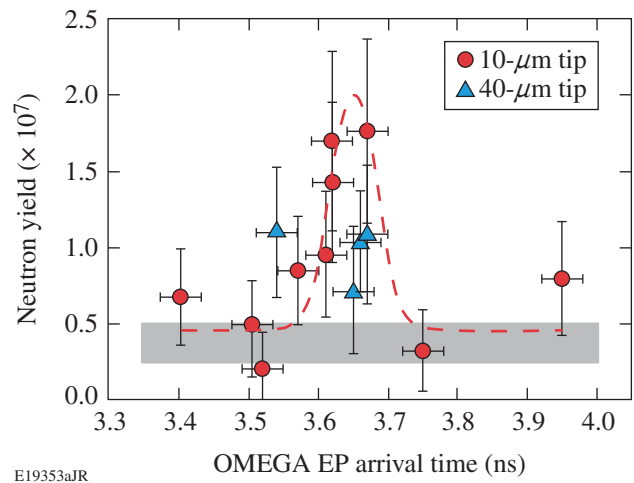
Figure 125.19
Measured neutron yield as a function of the arrival time of the short-pulse laser for two types of cone targets: 10-μm (circles) and 40-μm (triangles) tip diameter. The gray area represents data without the short-pulse laser.

larger tip (40 μm). The 10-μm data show a peak in neutron yield at a delay time of 3.65±0.02 ns. Most of the tips were 15 μm thick. The dashed curve is a fit of a Gaussian profile to the red circles. The gray bar shows the yield from several shots without the short-pulse beam, measured with a different detector that had smaller yield error. Most of the null shots were taken with the 10-μm-flat-tip cone target, but some null shots were also taken with the 40-μm flat tip. The same implosion yield was measured within the measurement uncertainty. The error bars include the error caused by neutron statistics and the cross-calibration error. The uncertainty in yield without the OMEGA EP pulse, indicated by the width of the gray bar, is lower because it represents an average over many shots using the more-accurate detector. The 10-μm data show an enhancement in neutron yield by more than a factor of 4 for the smaller-tip targets and a properly timed short-pulse beam. The experiments measured $(1.4±0.6) \times 10^7$ additional neutrons resulting from heating by the short-pulse laser in a narrow time window of less than 100 ps. This corresponds to a coupling efficiency of 3.5±1.0% of the short-pulse energy into the core.[36]

It is expected that most of the OMEGA EP beam energy interacted with the side walls of the cone in the smaller-tip target, while a significant portion of laser energy interacted under normal incidence with the circular flat in the larger tip. It is surprising that the data from the larger tip may indicate a lower coupling efficiency. However, only four shots have been taken with this target type to date and more experiments are required covering a larger time range of OMEGA EP arrival times. The neutron peak might be shifted for the 40-μm tip. Hydrodynamic simulations are very similar for both targets and timing shifts of more than 50 ps are not expected. Possible causes for the difference in neutron yield are higher fast-electron conversion efficiency in the smaller tip and better electron transport. Intense laser–plasma interaction with cone-like structures might lead to a higher conversion efficiency into fast electrons[37] and enhanced surface acceleration of fast electrons.[38] It is expected that the density scale length plays an important role in the conversion efficiency and the directionality of the fast electrons.[39] A better understanding requires characterization of the preplasma (see below) and PIC simulations of the laser–plasma interaction.

Fast electrons that escaped the target were measured in two different directions with two absolutely calibrated electron spectrometers based on permanent magnets and image plates.[40] The spectrometers covered the energy range from 0.1 to 100 MeV. Figure 125.20 shows measured spectra in the laser's forward direction and sideways (at an angle of 79° to
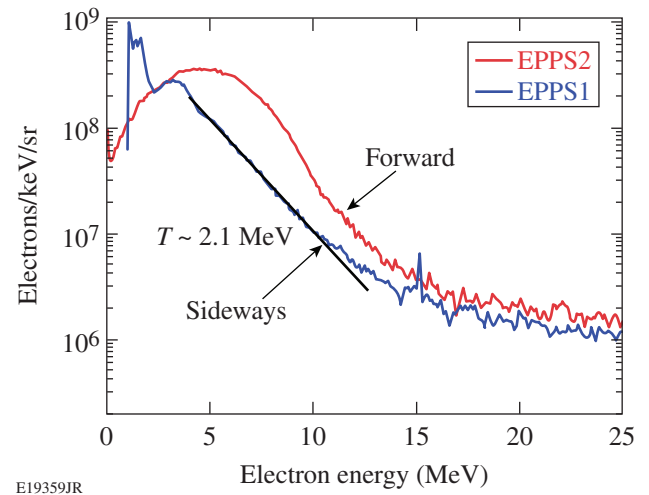

Figure 125.20
Fast-electron spectra measured in the laser's forward direction (red curve) and perpendicular to the laser direction (blue curve) (shot 59124).

the laser axis). The spectra were measured simultaneously. Significant numbers of electrons were measured with kinetic energies up to several tens of MeV in both directions. The total number of escaped electrons was ~40% higher in the forward direction. The mean energy averaged over the whole range was ~5.1 MeV in the forward direction and ~3.7 MeV sideways. The slope temperature of the sideways curve is about 2 MeV in the 5- to 10-MeV range and is significantly higher than that expected based on ponderomotive scaling of the average laser intensity in vacuum. It is interesting to note that in the range up to 2 MeV, ~10× more fast electrons are measured sideways. This might be caused by the forward-generated electrons as they are stopped in the dense fuel assembly. Another possible explanation is that strong self-generated electric and magnetic fields affect the directionality of the emitted electrons.[41,42]

The energy spectrum of the escaped electrons is only indirectly related to that of the generated electrons.[42] A few percent of the electrons are able to escape the target through the large Debye sheath fields that are formed at the plasma boundary. Escaping electrons lose energy to the sheath potential, which is a function of time, and therefore the spectrum of the escaping electrons is modified. Assuming that the forward-electron component is emitted into a cone with a 45° half-angle and that the colder distribution is emitted sideways from 90° to 45° with respect to the laser direction, it is estimated that the total energy carried away by the fast electrons is ~7.3 J, which corresponds to ~0.8% of the OMEGA EP pulse energy. Assuming a conversion efficiency of ~20% to 30% of laser energy into fast electrons,[23,43] a few percent of the fast electrons escaped

the target as expected. The estimate is not very sensitive on the half-angle of the forward-going component. For example, a total energy of ~5.8 J is estimated for a 10° half-angle.

The higher electron energies may be caused by cone filling by a preplasma. Self-focusing and beam filamentation in this preplasma seeded by the OMEGA EP beam nonuniformities may explain the observed hard electron spectrum.[24] Filamentary structures in an under-dense plasma with periodicity orthogonal to the laser beam direction can be driven by thermal,[44] ponderomotive,[45] and relativistic effects.[46] The last two are probably the dominant effects for the present experiment. An incident light beam that is slightly more intense in one region results in a lateral force, pushing the plasma electrons sideways from the region of highest laser intensity and leaving behind a region of lower electron density, n_e. This results in a transversal modulation of the index of refraction, $n = \sqrt{1 - n_e/n_c}$, where n_c is the critical density. The slightly increased index of refraction in the depleted region causes the wave front to curve in such a way that light is focused into the region of high intensity, which is counteracted by diffraction. The process leads to a positive feedback and results into what is known as the filamentation instability. Filamentation and self-focusing can therefore lead to much higher laser intensities than in vacuum and produce a hotter electron population, which was observed in this experiment. Some portion of the laser light may be transported in these filaments, at higher intensities, deeper into the preplasma. This effect was observed in 2-D PIC simulations for similar experimental conditions.[24]

Integrated Simulations and Discussion

DRACO[47] + *LSP*[48] simulations were performed to estimate the coupling of fast electrons to the compressed CD.[36] *DRACO* simulated the fuel assembly in cylindrical geometry and was coupled with the implicit hybrid PIC code *LSP* to calculate the fast-electron propagation and energy deposition in the target.[4,10] In the simulation, the Au cone tip had an inner diameter of 40 μm, a wall thickness of 15 μm, and a cone half-angle of 37°. The cone tip was 55 μm away from the center of the shell. The laser–plasma interaction was not modeled. The simulation assumed a fast-electron beam that was promoted from thermal electrons at the inside of the cone wall with an initial full-angle spread of 110°. Various experimental[49,50] and theoretical work[51] indicates that a full angle of about 100° for the MeV electrons is a reasonable number for the initial divergence angle. The electron-transport calculation through the gold cone included scattering. Similar to the experimental observation, the injection time of the fast electrons was chosen ~50 ps before shock breakout at a time when the shock wave was transiting through the cone wall. An exponential energy distribution was assumed for the fast electrons with a mean energy given by the maximum of the ponderomotive[52] and Beg[53] scalings. The total energy of the fast electrons generated at the inside cone wall contained 16% of the OMEGA EP beam energy with a fast-electron temperature of ~0.3 MeV.

Initial *DRACO* runs without the OMEGA EP beam yielded higher neutron numbers than measured, indicating higher density and temperature in the simulation. The fusion-reaction rate is highly sensitive to the density and temperature distribution in the assembled fuel. Beside an over-predicted density, mainly the higher temperature leads to a higher yield because the fusion reactivity roughly varies with the fourth power of the ion temperature in the range of interest. A number of effects contribute to the over-prediction. Radiation transport was not included and a uniform drive over the shell was assumed that is too optimistic. Low-adiabat implosions with plastic shells and high-convergence ratio are strongly RT instable during the deceleration phase, giving rise to mixing of cold-shell material into hotter parts of the plasma, which quenches the fusion reaction and leads to lower temperatures than predicted.[18] The presence of the cone also leads to a reduction in ion temperature. Neutron and proton measurements from D^3He-filled cone-in-shell targets have shown that measured ion temperatures are a factor of 2 lower than predicted, while ρR is reduced by only 30%.[26] This shows that the cone affects the ion temperature much more than ρR. The ion temperature was, therefore, reduced in the simulation to obtain a neutron yield consistent with the experiment. To match the neutron yield when the OMEGA EP beam is not fired, the temperature had to be reduced by a factor of 2.1 in the shell and a factor of 1.4 in the plasma region in front of the cone tip, which was heated by a shock that bounced back from the cone tip.

Figure 125.21(a) shows the ion temperature of the target without and with hot-electron heating. The simulation shows that the imploded shell material was pushed against the cone tip and was heated strongly up to ~2 keV. Fast electrons deposited more than 50% of their energy in the cone wall, which was strongly heated. Radiation cooling was not included in the simulation, and the temperature in gold was artificially clamped to 1 keV. Most of the fast electrons that were transmitted through the cone wall deposited their energy in the lower-density plasma (>2 g/cm³) close to the tip of the cone between the tip and the core. From Fig. 125.21(b), the peak neutron-production density occurred at the core in the absence of hot electrons. With hot electrons, the neutron-production density is largest just to the left of the tip of the cone ($Z \approx 60$ μm). The simulation obtained
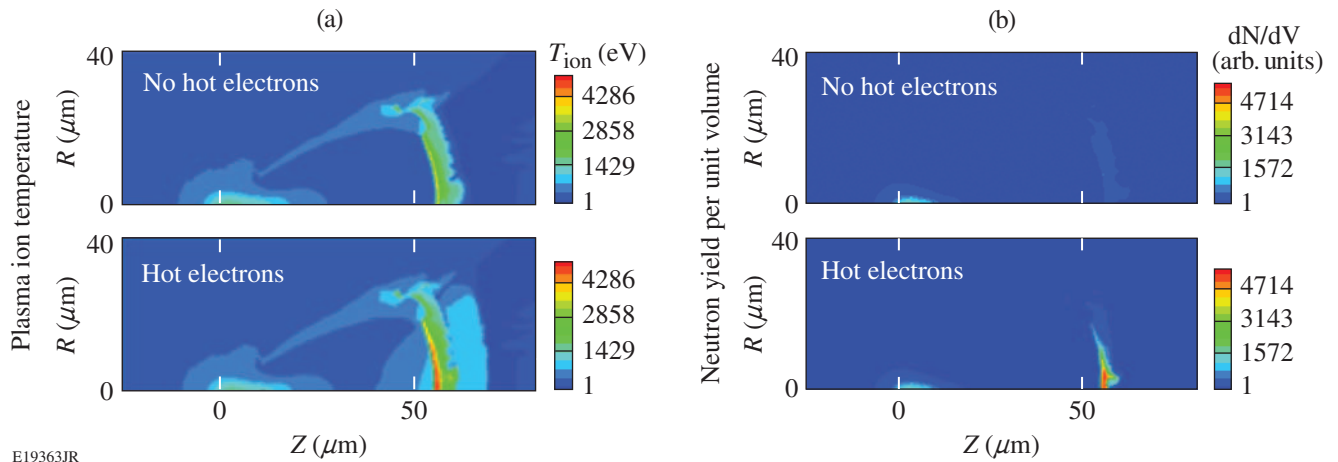
Figure 125.21
DRACO + LSP simulation for a 10-ps, 1.0-kJ, $R_{80} = 27$-μm OMEGA EP pulse, showing contours of (a) plasma ion temperature and (b) neutron yield per unit volume, with and without hot electrons produced by the OMEGA EP pulse.

a neutron-yield enhancement of 1.4×10^7, which required that $3.5\pm1.0\%$ of the OMEGA EP energy was coupled into the CD by fast electrons. Some fraction of fast electrons left the target without significant heating. According to the simulation, only about 0.4% of the OMEGA EP energy coupled to densities above 100 g/cm^3.

The current results are now compared to previous integrated experiments. An integrated experiment performed on Rutherford Appleton Laboratory's VULCAN Laser studied the flux of high-intensity laser-generated electrons via a hollow cone into a laser-imploded plasma.[42] The shell was imploded by six 900-J, 1-ns laser beams at 1.05-μm wavelength, and a 10-ps, 70-J laser pulse was focused into a hollow Au cone with a peak intensity of $\sim3 \times 10^{18}$ W/cm^2 in vacuum. The compressed densities and areal densities were more than an order of magnitude lower than in the present case. The cone had similar dimensions with a tip thickness of 10 μm. The flux of high-energy electrons traversing the imploded CD was determined from comparing the measured K$_\alpha$ fluorescence yield from a Cu dopant in the shell to Monte Carlo simulations that modeled the fast-electron transport in the CD and calculations of the K$_\alpha$ yield. It was estimated that $\sim7\%$ to 22% of the short-pulse laser energy was converted into fast electrons in the CD, depending on the assumed hot-electron temperature.[42] This number seems higher than what is reported here, but electron-transport modeling indicates that only a small fraction of the fast-electron energy ($\sim9\%$) was actually deposited into the CD in the VULCAN experiment. The model in Ref. 42 did not include the physics of electron transport in the cone wall, which might affect the inferred coupling efficiency. Our modeling shows that fast-

electron transport is very sensitive to scattering in the high-Z material and is influenced by resistive magnetic fields at the high-Z cone walls.[36]

Integrated experiments were performed about a decade ago on the GEKKO XII Laser System in Japan.[12] A 500-μm-diam, 7-μm-thick CD shell was imploded by nine beams at a wavelength of 0.53 μm and with an energy of 2.5 kJ with 1.2-ns, flat-top pulses. The compressed density was estimated with 50 to 100 g/cm^3. Similar peak densities were obtained in our experiment but with significantly higher drive energy and a shaped UV drive pulse. No shock-breakout measurements were reported in Ref. 12. With a 300-J, 0.6-ps (0.5-PW) heating beam, $\sim2 \times 10^7$ neutrons were reported compared to 2 to 5×10^4 with no heating beam. The time window in which the enhancement was observed was ~80 ps, which is very similar to our measurement. Simple predictions of the neutron yield normalized to the yield without heating were used to derive a coupling of 15% to 30% of laser energy to core heating.[12] These numbers are considerably higher than the number reported here. The coupling efficiency here is based on comparing the measured heating neutron yield to more sophisticated integrated simulations that include the hydrodynamics and the fast-electron transport through the cone wall and into the fuel assembly. Possible explanation of the difference in coupling efficiency is a different level of preplasma formation.

Recent integrated experiments at GEKKO XII with the new LFEX short-pulse laser[54] were not able to reproduce the previous results and measured neutron yields are significantly lower.[55] This is attributed to the formation of a preplasma in the

cone by a laser prepulse or pedestal. Short-pulse experiments with cone-like structures on the TITAN Laser at LLNL and on the LULI 100 TW Laser in France revealed the presence of preplasma over 100 μm away from the cone tip for very similar laser contrast.[56,57] It was shown in Ref. 24 that a preformed plasma in a hollow cone strongly influences the ultra-intense laser–plasma interaction and the hot-electron generation. The laser beam filamented in the underdense plasma and the laser energy was diverted from the cone tip for large preplasmas. The laser beam propagation halted and energetic electrons were generated mostly transverse to the incoming beam.[24]

Two-dimensional simulations were performed with the radiation–hydrodynamics code *HYDRA*[58] to study the preplasma formation for the present case using the measured prepulse. Figure 125.22 shows the simulated density contours for the smaller tip diameter. A preplasma fills the cone, and the nonrelativistic critical density shifts ~100 μm away from the original position of the inner cone wall at the time when the main pulse is incident. Results for the larger tip were similar but had slight differences in the shape of the density contours. An experimental characterization of the preplasma in the cone is important and will be performed in the future.
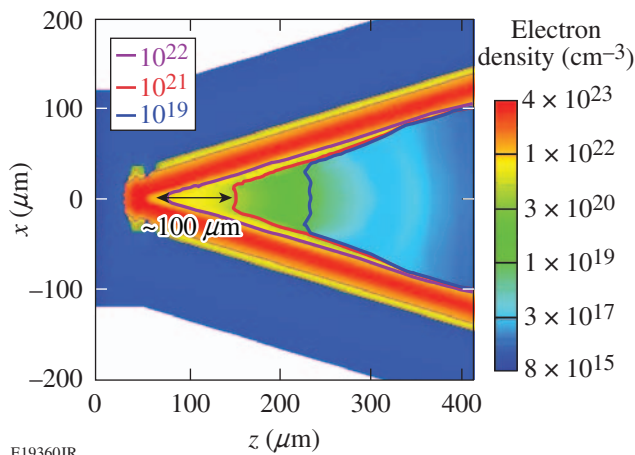

E19360JR

Figure 125.22
Electron-density contours from a 2-D *HYDRA* simulation at the time of the short-pulse interaction of the preplasma formation in a gold cone with inner tip diameter of 10 μm.

The integrated simulations were based on the assumption of a relatively low fast-electron temperature from the average intensity in vacuum. More heating of the dense portion of the core is expected with a hotter-electron distribution, which is expected from laser interactions with a preformed plasma. This requires large-scale PIC simulations that model the details of the laser–preplasma interaction and couple these results to the integrated simulations. Such large-scale PIC simulations will be performed in the future.

Summary

The fast-ignitor, cone-in-shell target concept has been investigated at the OMEGA Laser Facility. Initial integrated fast-ignition experiments with room-temperature re-entrant cone targets were performed using a shaped laser pulse to implode the capsule with 20 kJ of UV energy on a low adiabat, followed by a 1-kJ, 10-ps, short-pulse IR beam interacting with a hollow gold cone at various times with respect to the driver laser.

Shock-breakout measurements have been performed with cone-in-shell targets under the same drive conditions, but without the short-pulse laser. The measurements confirm an intact cone tip at the time of peak neutron production in the integrated shots. VISAR measurements show that Au cones with a thin tip (5 μm) are affected by x-ray preheat that is produced in the corona of the imploding shell. This leads to premature material release inside the hollow cone, which might affect the short-pulse laser interaction. The thicker cone walls (15 μm Au) that were used in the integrated shots are well shielded against the x rays and are not affected by preheat.

In the integrated shots, a fourfold increase in neutron yield was observed by short-pulse heating in a narrow (~100-ps) time window close to peak compression. The additional $(1.4\pm0.6)\times 10^7$ neutrons produced by the short-pulse beam correspond to a coupling efficiency of 3.5±1.0% of short-pulse energy into the CD, according to simulations with the integrated *DRACO + LSP* codes.

Electrons with energies higher than 20 MeV were measured in the direction of the short-pulse laser and perpendicular to it. More escaping electrons were measured in the forward direction, integrated over the whole energy range, but for energies below 2 MeV a significant depletion was observed in the spectrum through the dense plasma.

Integrated simulations show significant target heating in the lower-density CD plasma adjacent to the cone tip, which is where most of the additional neutrons are created. The simulations assumed a hot-electron temperature based on ponderomotive scaling of the laser intensity in vacuum and no preplasma. Additional two-dimensional hydrodynamic simulations using the measured laser prepulse indicate a significant production of preplasma in the cone. Laser interaction with and filamentation in a lower-density preplasma might consequently lead to much

higher laser intensities and produce a hotter-electron distribution. There is evidence for this from the measured spectra of escaped electrons showing significantly higher mean energy than expected.

This work addresses a number of important issues for fast ignition, which include cone survivability and the tradeoff of matching the cone thickness to the fast-electron energy. More work must be done to optimize the target geometry and materials. This also includes improvements in the short-pulse–laser contrast, a smaller focus, and a higher energy. It is expected that these improvements will increase the coupling efficiency and lead to a greater enhancement in the number of neutrons. Simulations were performed with a smaller focus ($R_{80} = 15\ \mu$m) and higher laser energy (2.6 kJ) without contrast degradation, leading to a fourfold increase in coupling efficiency to densities above 100 g/cm^3. Integrated experiments with improved laser parameters will be performed in the future.

ACKNOWLEDGMENT

REFERENCES

1. N. G. Basov, S. Yu. Gus'kov, and L. P. Feokistov, J. Sov. Laser Res. **13**, 396 (1992).

2. M. Tabak *et al.*, Phys. Plasmas **1**, 1626 (1994).

3. R. Betti and C. Zhou, Phys. Plasmas **12**, 110702 (2005).

4. A. A. Solodov, K. S. Anderson, R. Betti, V. Gotcheva, J. Myatt, J. A. Delettrez, S. Skupsky, W. Theobald, and C. Stoeckl, Phys. Plasmas **15**, 112702 (2008).

5. S. Atzeni *et al.*, Phys. Plasmas **15**, 056311 (2008).

6. J. J. Honrubia and J. Meyer-ter-Vehn, Plasma Phys. Control. Fusion **51**, 014008 (2009).

7. A. J. Kemp, Y. Sentoku, and M. Tabak, Phys. Rev. Lett. **101**, 075004 (2008).

8. J. R. Davies *et al.*, Phys. Rev. E **56**, 7193 (1997).

9. A. R. Bell and R. J. Kingham, Phys. Rev. Lett. **91**, 035003 (2003).

10. A. A. Solodov, K. S. Anderson, R. Betti, V. Gotcheva, J. F. Myatt, J. A. Delettrez, S. Skupsky, W. Theobald, and C. Stoeckl, Phys. Plasmas **16**, 056309 (2009).

11. P. A. Norreys *et al.*, Phys. Plasmas **7**, 3721 (2000).

12. R. Kodama *et al.*, Nature **412**, 798 (2001); R. Kodama *et al.*, Nature **418**, 933 (2002).

13. T. R. Boehly, D. L. Brown, R. S. Craxton, R. L. Keck, J. P. Knauer, J. H. Kelly, T. J. Kessler, S. A. Kumpan, S. J. Loucks, S. A. Letzring, F. J. Marshall, R. L. McCrory, S. F. B. Morse, W. Seka, J. M. Soures, and C. P. Verdon, Opt. Commun. **133**, 495 (1997).

14. L. J. Waxer, D. N. Maywar, J. H. Kelly, T. J. Kessler, B. E. Kruschwitz, S. J. Loucks, R. L. McCrory, D. D. Meyerhofer, S. F. B. Morse, C. Stoeckl, and J. D. Zuegel, Opt. Photonics News **16**, 30 (2005).

15. V. N. Goncharov, T. C. Sangster, T. R. Boehly, S. X. Hu, I. V. Igumenshchev, F. J. Marshall, R. L. McCrory, D. D. Meyerhofer, P. B. Radha, W. Seka, S. Skupsky, C. Stoeckl, D. T. Casey, J. A. Frenje, and R. D. Petrasso, Phys. Rev. Lett. **104**, 165001 (2010).

16. General Atomics, San Diego, CA, 92123.

17. C. Stoeckl, T. R. Boehly, J. A. Delettrez, S. P. Hatchett, J. A. Frenje, V. Yu. Glebov, C. K. Li, J. E. Miller, R. D. Petrasso, F. H. Séguin, V. A. Smalyuk, R. B. Stephens, W. Theobald, B. Yaakobi, and T. C. Sangster, Phys. Plasmas **14**, 112702 (2007).

18. C. D. Zhou, W. Theobald, R. Betti, P. B. Radha, V. A. Smalyuk, D. Shvarts, V. Yu. Glebov, C. Stoeckl, K. S. Anderson, D. D. Meyerhofer, T. C. Sangster, C. K. Li, R. D. Petrasso, J. A. Frenje, and F. H. Séguin, Phys. Rev. Lett. **98**, 025004 (2007).

19. T. R. Boehly, V. A. Smalyuk, D. D. Meyerhofer, J. P. Knauer, D. K. Bradley, R. S. Craxton, M. J. Guardalben, S. Skupsky, and T. J. Kessler, J. Appl. Phys. **85**, 3444 (1999).

20. Y. Lin, T. J. Kessler, and G. N. Lawrence, Opt. Lett. **21**, 1703 (1996).

21. W. Theobald, K. S. Anderson, R. Betti, R. S. Craxton, J. A. Delettrez, J. A. Frenje, V. Yu. Glebov, O. V. Gotchev, J. H. Kelly, C. K. Li, A. J. MacKinnon, F. J. Marshall, R. L. McCrory, D. D. Meyerhofer, J. F. Myatt, P. A. Norreys, P. M. Nilson, P. K. Patel, R. D. Petrasso, P. B. Radha, C. Ren, T. C. Sangster, W. Seka, V. A. Smalyuk, A. A. Solodov, R. B. Stephens, C. Stoeckl, and B. Yaakobi, Plasma Phys. Control. Fusion **51**, 124052 (2009).

22. J. Bromage, S.-W. Bahk, D. Irwin, J. Kwiatkowski, A. Pruyne, M. Millecchia, M. Moore, and J. D. Zuegel, Opt. Express **16**, 16561 (2008).

23. P. M. Nilson, A. A. Solodov, J. F. Myatt, W. Theobald, P. A. Jaanimagi, L. Gao, C. Stoeckl, R. S. Craxton, J. A. Delettrez, B. Yaakobi, J. D. Zuegel, B. E. Kruschwitz, C. Dorrer, J. H. Kelly, K. U. Akli, P. K. Patel, A. J. MacKinnon, R. Betti, T. C. Sangster, and D. D. Meyerhofer, Phys. Rev. Lett. **105**, 235001 (2010).

24. A. G. MacPhee *et al.*, Phys. Rev. Lett. **104**, 055002 (2010).

25. C. Dorrer, D. Irwin, A. Consentino, and J. Qiao, presented at the ICUIL 2010 Conference, Watkins Glen, NY, 26 September–1 October 2010 (Paper ThO3).

26. C. Stoeckl, T. R. Boehly, J. A. Delettrez, S. P. Hatchett, J. A. Frenje, V. Yu. Glebov, C. K. Li, J. E. Miller, R. D. Petrasso, F. H. Séguin, V. A.

Smalyuk, R. B. Stephens, W. Theobald, B. Yaakobi, and T. C. Sangster, Plasma Phys. Control. Fusion **47**, B856 (2005).

27. J. E. Miller, T. R. Boehly, A. Melchior, D. D. Meyerhofer, P. M. Celliers, J. H. Eggert, D. G. Hicks, C. M. Sorce, J. A. Oertel, and P. M. Emmel, Rev. Sci. Instrum. **78**, 034903 (2007).

28. P. M. Celliers, D. K. Bradley, G. W. Collins, D. G. Hicks, T. R. Boehly, and W. J. Armstrong, Rev. Sci. Instrum. **75**, 4916 (2004).

29. R. S. Craxton and R. L. McCrory, J. Appl. Phys. **56**, 108 (1984).

30. J. Delettrez, R. Epstein, M. C. Richardson, P. A. Jaanimagi, and B. L. Henke, Phys. Rev. A **36**, 3926 (1987); M. C. Richardson, P. W. McKenty, F. J. Marshall, C. P. Verdon, J. M. Soures, R. L. McCrory, O. Barnouin, R. S. Craxton, J. Delettrez, R. L. Hutchison, P. A. Jaanimagi, R. Keck, T. Kessler, H. Kim, S. A. Letzring, D. M. Roback, W. Seka, S. Skupsky, B. Yaakobi, S. M. Lane, and S. Prussin, in *Laser Interaction and Related Plasma Phenomena*, edited by H. Hora and G. H. Miley (Plenum Publishing, New York, 1986), Vol. 7, pp. 421–448.

31. D. R. Lide, *CRC Handbook of Chemistry and Physics*, 82nd ed. (CRC Press, Boca Raton, FL, 2001), p. 4-132.

32. W. Theobald, J. E. Miller, T. R. Boehly, E. Vianello, D. D. Meyerhofer, T. C. Sangster, J. Eggert, and P. M. Celliers, Phys. Plasmas **13**, 122702 (2006).

33. C. Stoeckl, M. Cruz, V. Yu. Glebov, J. P. Knauer, R. Lauck, K. Marshall, C. Mileham, T. C. Sangster, and W. Theobald, Rev. Sci. Instrum. **81**, 10D302 (2010); R. Lauck *et al.*, IEEE Trans. Nucl. Sci. **56**, 989 (2009).

34. V. Yu. Glebov, C. Stoeckl, T. C. Sangster, S. Roberts, G. J. Schmid, R. A. Lerche, and M. J. Moran, Rev. Sci. Instrum. **75**, 3559 (2004).

35. F. J. Marshall, J. A. Delettrez, R. Epstein, V. Yu. Glebov, D. R. Harding, P. W. McKenty, D. D. Meyerhofer, P. B. Radha, W. Seka, S. Skupsky, V. A. Smalyuk, J. M. Soures, C. Stoeckl, R. P. Town, B. Yaakobi, C. K. Li, F. H. Séguin, D. G. Hicks, and R. D. Petrasso, Phys. Plasmas **7**, 2108 (2000).

36. W. Theobald, A. A. Solodov, C. Stoeckl, K. S. Anderson, R. Betti, T. R. Boehly, R. S. Craxton, J. A. Delettrez, C. Dorrer, J. A. Frenje, V. Yu. Glebov, H. Habara, K. A. Tanaka, J. P. Knauer, R. Lauck, F. J. Marshall, K. L. Marshall, D. D. Meyerhofer, P. M. Nilson, P. K. Patel, T. C. Sangster, W. Seka, N. Sinenian, T. Ma, F. N. Beg, and R. B. Stephens, "Integrated Fast-Ignition Core-Heating Experiments on OMEGA," submitted to Physical Review Letters.

37. W. Theobald, V. Ovchinnikov, S. Ivancic, B. Eichman, P. M. Nilson, J. A. Delettrez, R. Yan, G. Li, F. J. Marshall, D. D. Meyerhofer, J. F. Myatt, C. Ren, T. C. Sangster, C. Stoeckl, J. D. Zuegel, L. Van Woerkom, R. R. Freeman, K. U. Akli, E. Giraldez, and R. B. Stephens, Phys. Plasmas **17**, 103101 (2010).

38. H. Habara *et al.*, Phys. Rev. Lett. **97**, 095004 (2006).

39. M. I. K. Santala *et al.*, Phys. Rev. Lett. **84**, 1459 (2000).

40. H. Chen *et al.*, Rev. Sci. Instrum. **79**, 10E533 (2008).

41. T. Yabuuchi *et al.*, New J. Phys. **11**, 093031 (2009).

42. M. H. Key, J. C. Adam, K. U. Akli, M. Borghesi, M. H. Chen, R. G. Evans, R. R. Freeman, H. Habara, S. P. Hatchett, J. M. Hill, A. Heron, J. A. King, R. Kodama, K. L. Lancaster, A. J. MacKinnon, P. Patel, T. Phillips, L. Romagnani, R. A. Snavely, R. Stephens, C. Stoeckl, R. Town, Y. Toyama, B. Zhang, M. Zepf, and P. A. Norreys, Phys. Plasmas **15**, 022701 (2008).

43. C. D. Chen *et al.*, Phys. Plasmas **16**, 082705 (2009).

44. O. Willi and P. T. Rumsby, Opt. Commun. **37**, 45 (1981).

45. B. I. Cohen and C. E. Max, Phys. Fluids **22**, 1115 (1979).

46. C. Max, J. Arons, and A. B. Langdon, Phys. Rev. Lett. **33**, 209 (1974).

47. P. B. Radha, T. J. B. Collins, J. A. Delettrez, Y. Elbaz, R. Epstein, V. Yu. Glebov, V. N. Goncharov, R. L. Keck, J. P. Knauer, J. A. Marozas, F. J. Marshall, R. L. McCrory, P. W. McKenty, D. D. Meyerhofer, S. P. Regan, T. C. Sangster, W. Seka, D. Shvarts, S. Skupsky, Y. Srebro, and C. Stoeckl, Phys. Plasmas **12**, 056307 (2005).

48. D. R. Welch *et al.*, Nucl. Instrum. Methods Phys. Res. A **464**, 134 (2001).

49. M. Storm, A. A. Solodov, J. F. Myatt, D. D. Meyerhofer, C. Stoeckl, C. Mileham, R. Betti, P. M. Nilson, T. C. Sangster, W. Theobald, and C. Guo, Phys. Rev. Lett. **102**, 235004 (2009).

50. J. S. Green, V. M. Ovchinnikov, R. G. Evans, K. U. Akli, H. Azechi, F. N. Beg, C. Bellei, R. R. Freeman, H. Habara, R. Heathcote, M. H. Key, J. A. King, K. L. Lancaster, N. C. Lopes, T. Ma, A. J. MacKinnon, K. Markey, A. McPhee, Z. Najmudin, P. Nilson, R. Onofrei, R. Stephens, K. Takeda, K. A. Tanaka, W. Theobald, T. Tanimoto, J. Waugh, L. Van Woerkom, N. C. Woolsey, M. Zepf, J. R. Davies, and P. A. Norreys, Phys. Rev. Lett. **100**, 015003 (2008).

51. C. Ren *et al.*, Phys. Plasmas **13**, 056308 (2006).

52. S. C. Wilks and W. L. Kruer, IEEE J. Quantum Electron. **33**, 1954 (1997).

53. F. N. Beg *et al.*, Phys. Plasmas **4**, 447 (1997).

54. J. Kawanaka *et al.*, J. Phys., Conf. Ser. **112**, 032006 (2008).

55. H. Azechi, Bull. Am. Phys. Soc. **55**, 291 (2010).

56. L. Van Woerkom *et al.*, Phys. Plasmas **15**, 056304 (2008).

57. S. D. Baton *et al.*, Phys. Plasmas **15**, 042706 (2008).

58. M. M. Marinak *et al.*, Phys. Plasmas **3**, 2070 (1996).